ACS OMEGA

Open Access

http://pubs.acs.org/journal/acsodf

Article

Dynamical Signatures of *Thermotoga maritima* Maltose-Binding Proteins Affected by Ligand Binding

Shantanu Shukla, Laura-Roxana Stingaciu,* Christopher Stanley, Pratul Agarwal, Matthew Cuneo, Andreas M. Stadler, and Dean Myles

Cite This: *ACS Omega* 2025, 10, 41446−41456

Read Online

ACCESS | Metrics & More | Article Recommendations

ABSTRACT: Functional segregation among protein isoforms depends on the interplay of their overall structures and the molecular dynamics of these structures. *Thermotoga maritima* maltose-binding protein (tmMBP) isoforms show size-dependent differential binding of maltose and malto-oligomers while maintaining remarkable fold conservation. This differential behavior needs detailed characterization in native-like aqueous conditions to understand the effects of protein dynamics on ligand binding and recognition. Small-angle neutron scattering (SANS), neutron spin echo (NSE) spectroscopy, and dynamic light scattering (DLS) were used in conjunction with previously published computational molecular dynamics (MD) simulations to understand the dynamic behavior of tmMBPs experimentally. SANS provided information on the overall structure of the molecules, while NSE was used to determine the dynamics in the nanosecond time scale. Both tmMBP2 and tmMBP3 have a bidomain architecture linked with a flexible hinge, with the binding pocket sitting in the cleft between the two domains. tmMBP2 and tmMBP3 showed different solution dynamics, with the translational and rotational components dominating the dynamics of both systems, resulting in a clear differentiation of their diffusion pattern. A faster dynamics component was also observed and was attributed to segmental dynamics. Differences observed between the ligand-free (apo) and ligand-bound (holo) states of the two proteins are attributed to conformational entropy. Our results highlight the intricacies of how structure and dynamics can together shape binding to a repertoire of substrates in structurally similar proteins.

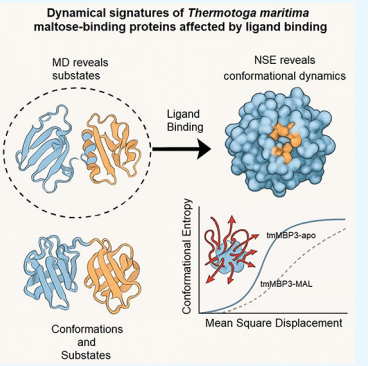

INTRODUCTION

Proteins are dynamic and undergo specific conformational changes in response to stimuli such as reaction to light, binding to a substrate or ligand, or changes in the physiochemical environment that further modulate and complicate the dynamic landscape of functional states. Molecular dynamics plays an essential role in the regulation of the biochemical function of enzymes or the binding affinity of a ligand to its protein binding partner. From a thermodynamic perspective, protein−ligand binding is characterized by a fragile balance between the enthalpy and entropy of the system regulated by the difference in Gibbs free energy between the ligand-bound and ligand-free states of the protein. Ligand−protein interactions can either increase or reduce the flexibility of the ligand−protein complex compared to the ligand-free proteins. The increase of protein flexibility upon ligand-binding results in a gain of conformational entropy, which stabilizes the bound state, while a reduction of protein motions in the ligand−protein complex results in a loss of conformational entropy, which is thermodynamically unfavorable. While the enthalpic contributions can be derived based on high-resolution structures, knowledge of the protein dynamics requires the use of high-resolution spectroscopic methods and adequate models to investigate protein systems.

Several protein systems have emerged as essential paradigm models for experimental, computational, and theoretical analyses of the protein dynamical landscape. One such system, the periplasmic binding proteins (PBPs), is ubiquitous in bacteria where they operate in conjunction with adenosine triphosphate binding cassette (ABC) transport systems to bind and translocate a diverse array of metabolites across the bacterial membrane. PBPs exhibit strong structural conservation, even when sequence similarities are low, and are characterized by a two-domain architecture in which the N- and C-terminal domains are connected by a flexible linker region that serves as a hinge.[1,2] Substrate binding occurs at the interface of these two domains, through which the flexible hinge switches from an open configuration to a closed

Received: May 20, 2025
Revised: August 20, 2025
Accepted: August 26, 2025
Published: September 3, 2025

configuration that captures the ligand at the interface. The degree and extent of these substrate-dependent domain motions characterize the PBP family. Across bacterial genera, substrate binding affinities are selectively tuned to the local milieu of the host organism, which can result in differing affinity profiles for identical ligands in respective cellular environments.[1−5] This is achieved by tailoring nonbonded interactions in and around the ligand binding sites and through conformational dynamics that can help fine-tune the thermodynamics and kinetics of ligand binding.[2,5,6] Moreover, some PBPs exhibit inbuilt allosteric mechanisms that modulate the affinity profiles for preferred ligands by controlling conformational switching between apo and substrate-bound states, properties that can be engineered to alter their ligand affinities.[7,8] Based on these findings, it is hypothesized that modulated changes in overall protein dynamics can provide a potential mechanism to encode broader functional diversity within a protein fold, beyond that attained by simply tuning molecular recognition through structural interactions in and around the binding pocket.[2,6]

Maltose-binding proteins (MBPs) serve as the primary receptors for alpha-linked glucose-based oligosaccharides, binding to malto-oligomers with varying affinity, typically at low micromolar concentrations. The MBP from *Escherichia coli* MBP (ecMBP) is the prototypical PBP, characterized in its apo-state as an open conformation that fluctuates on the nanosecond time scale between a major open and a minor partially closed conformation and by a switch upon ligand binding to closed forms that capture the substrate at the hinged interface between the two domains. Notably, ecMBP is very promiscuous, binding a variety of maltose-based ligands with markedly differing affinities mediated through a range of induced structural reorganizations and closed conformational states. Moreover, these binding interactions, which are generally enthalpically unfavorable, are favored by solvent release and local reordering at and around the binding site. The internal conformational dynamics associated with these type-specific ligand binding interactions thus serve as determinants of ligand affinity. While many other bacteria retain only a single copy of a more promiscuous MBP, some organisms maintain more than one MBP isoform. The hyperthermophile *Thermotoga maritima* maintains three isoforms of MBP (tmMBP1−3) that are high affinity receptors for di-, tri-, and tetra-saccharides, respectively.[9] tmMBP1 (391 residues) and tMBP2 (393 residues) share significant sequence identity (approximately 90%) but tmMBP3 (411 residues) shares less than 40% identity. The tmMBPs share roughly 35% sequence identity with ecMBP. Thus, this cluster of MBP isoforms offers an interesting opportunity to investigate the mechanisms underlying the evolution of specificity and affinity profiles in a genome where MBP gene redundancy is present.

In previously published work, we determined the X-ray crystal structures of tmMBP1, tmMBP2, and tmMBP3 in the absence and presence of substrates, to better understand how local binding interactions may modulate specificity and used solution-based small-angle X-ray scattering and microsecond time scale (500 ns) computer simulations and theoretical modeling to examine the contribution of conformational dynamics to the binding properties and behaviors encoded within each tmMBP isoform.[1] The results indicated that the interplay of structure and dynamics within these homologues are principal determinants of their substrate interaction profiles. Specifically, the study showed that tmMBP2 and tmMBP3 exhibit differential binding profiles based on the size of the cognate substrate, wherein tmMBP2 binds larger malto-oligomers and tmMBP3 binds only to maltose, and the published MD simulations[1] indicated the possibility of an underlying dynamical variation that may dictate the preferential ligand binding mode in the two isoforms.

To further investigate this hypothesis, the differences in the internal dynamic landscapes of the two structurally related isoforms, tmMBP2 and tmMBP3, were assessed by using neutron spin echo (NSE) spectroscopy. NSE spectroscopy has significant advantages over other experimental techniques commonly used to study protein dynamics. NSE spectroscopy can measure protein dynamics across broad time and length scales in a nondenaturing environment, which enables measurement in a near-native state. In NSE spectroscopy, the protein does not need to be tagged or altered and can thus provide a direct high-resolution method to measure various contributors to the overall dynamics of the protein. Due to a highly concentrated sample requirement for NSE, often above 50 mg/mL, the technique can also simulate the crowded environment inside the cells and can provide a more realistic picture of *in vivo* protein conformational changes. The NSE method measures dynamics in the picosecond to nanosecond time scales, similar to the time scales accessed by MD simulations.

Our present study provides differences between the dynamic states of two structurally related proteins performing divergent functions and identifies the subtle change in dynamics underlying biochemical events like ligand binding. We incorporated dynamic light scattering (DLS), small-angle neutron scattering (SANS), and NSE in conjunction with previously obtained computational MD simulations to examine the differences in the dynamic landscapes of two structurally related *Thermotoga* maltose-binding protein isoforms, tmMBP2 and tmMBP3. As stated before, the MD simulations indicated a possible underlying dynamical variation in the two isoforms that dictate a preferential ligand binding mode. The inherent structural conservation in these proteins and their marked complexity in size-dependent substrate selection make interesting targets to test theories of dynamics-mediated functional segregation in proteins. Here, we present data on both systems in the absence (apo) and presence (holo) of their cognate ligands. SANS was used to determine the overall shape of the proteins, while DLS and NSE were combined to determine translational diffusion and its contribution to overall dynamics and changes in rigidity due to the presence of cognate ligands. The previously published MD simulations provided a theoretical model to compare the NSE experimental dynamics profiles with the predominant modes during ligand binding events. Together, these techniques have helped differentiate the collective motions of the structurally related isoforms from their subtle segmental motions. They also demonstrate new ways to empirically detect and correlate the dynamics of structurally related proteins to help determine and interpret their differential mechanism of action.

MATERIALS AND METHODS

Molecular Dynamics Simulation. Twenty-one separate MD simulations were performed in 2018 on 21 tmMBP's systems from *Thermotoga maritima* (tmMBP1, tmMBP2, and tmMBP3) and *Escherichia coli* (ecMBP) bound to various glucose-based oligosaccharides substrates. Complete details of the MD simulations conditions and equilibration protocols

https://doi.org/10.1021/acsomega.5c04729
ACS Omega 2025, 10, 41446−41456

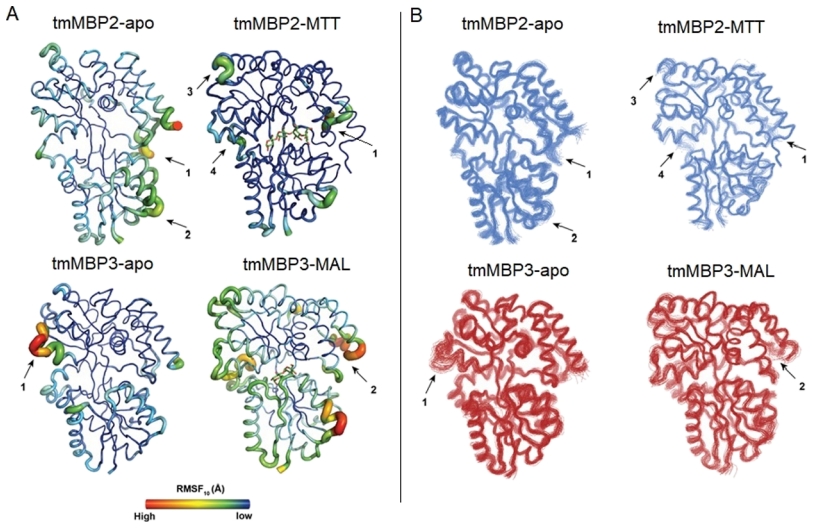

Figure 1. Conformational flexibility of tmMBP2 and tmMBP3 isoforms as shown by MD simulation results. (A) Root-mean-square fluctuations of the first 10 quasi-harmonic modes (RMSF10) computed and aggregated as a measure of the proteins flexibility: the width of the tube represents the sampled area of the residues; blue regions represent rigid or less flexible regions, whereas regions highlighted in red represent highly dynamic profiles. (B) Quasi-harmonics (QHA) of the top modes with the regions of interest marked.

were the subject of previously published studies and can be found in Shukla et al., 2018 and Gagné et al., 2016.[1,2] In the following, we summarize only the most relevant information for the systems in our study: tmMBP2 and tmMBP3. MD simulations on tmMBP2 and tmMBP3 in apo and holo-states were performed using AMBER[3,4] version 14 suite, in explicit water solvent. An SPC/E water model[5,10] was used to solvate a periodic rectangular box, with a 10 Å distance between protein and the edge of the box and a previously published equilibration protocol.[1,6] The final production run of 500 ns was performed under constant-energy conditions (NVE ensemble). The analysis of trajectories was performed using CPPTRAJ.[7] To identify global motions on slower time scales, the protein flexibility was characterized using quasi-harmonic analysis (QHA), and the first (slowest) 10 quasi-harmonic modes (RMSF10) were computed and aggregated as a measure of protein flexibility, denoted as root mean square fluctuations (RMSF10).[8] A total of 10,000 conformational snapshots from the last 100 ns of simulation time were finally saved and used for NSE analysis and coherent intermediate scattering function calculations.

Protein Expression and Purification. Both tmMBP2 and tmMBP3 were expressed and purified as per the protocol given in ref 1 with a few modifications. Briefly, both isoforms were grown in 3L of Enfors minimal media in a bioreactor at 32 °C until an O.D. of 20 was reached. The cells were then induced using 1 M IPTG and grown at 25 °C for overnight induction. Cell disruption by sonication was followed by incubation of the lysate at 80 °C for 15 min to get rid of any contaminating *Escherichia coli* proteins. The lysate was spun down, and the supernatant was subjected to a two-step purification process involving a His-tag affinity purification, followed by gel filtration. The collected fractions of purified protein were concentrated to approximately 51 mg/mL and were buffer exchanged with gel filtration buffer (20 mM Tris pH 7.5 and 40 mM NaCl) containing D_2O.

Small-Angle Neutron Scattering (SANS). SANS experiments were performed at the EQ-SANS beamline (BL-6) at the Spallation Neutron Source (SNS), Oak Ridge National Laboratory (ORNL).[11] Dialyzed tmMBP2 and tmMBP3 protein solutions in apo form: tmMBP2-apo and tmMBP3-apo, and substrate bound form: tmMBP2-MTT and tmMBP3-MAL (with MTT = maltotetraose for tmMBP2, and MAL = maltose for tmMBP3[9]), were used for SANS experiments in a five dilutions series: 1, 5, 10, 20, and 50 mg/mL. The generated data were background-corrected by using D_2O dialysis buffer. All the data sets were collected at 50 °C to match the NSE measurement. The Q-range explored during the SANS experiment was from ∼0.01 to ∼0.60 Å^{-1}. The relative scattering intensities $I(q)$ as a function of momentum transfer vector q ($q = 4\pi \sin \theta/\lambda$) was calculated by circular averaging of the scattered data. ATSAS[12,13] was used for the $P(r)$ analysis. Form factor per unit mass $F(q)$ was estimated by scaling the background-corrected scattering data and extrapolating it to the zero concentration for each q-value. The form factor $F(q)$ gives information about the shape of the molecule in a diluted solution. The structure factor, $S(q)$, describes the protein−protein interaction in high concentration solution and is calculated by dividing the concentration scaled scattering data $I(q)$ by $F(q)$. SANS was performed on samples from the same batch as later used for NSE experiments to maintain data consistency.

Dynamic Light Scattering. DLS experiments were performed using a DynaPro NanoStar (Wyatt Technology Corp.) at a scattering angle of 90°. 100 μL samples of dilutions ranging from 1 to 50 mg/mL were used for the experiment. The samples were centrifuged and filtered prior to the experiment to remove any large aggregates. The CONTIN algorithm in the DYNAMIC software was used to analyze the data and to identify polydispersity, molecular mass, and translational diffusion coefficient.[14−16] All measurements were performed at 50 °C.

Neutron Spin Echo (NSE) Spectroscopy. NSE experiments were performed on four samples (tmMBP2-apo, tmMBP3-apo, tmMBP2-MTT, and tmMBP3-MAL) at the SNS-NSE spectrometer at the Spallation Neutron Source, ORNL.[17] Quartz cells of 40 × 30 mm^2 and a path length of 4 mm were used to store ∼4 mL of protein solution. Three different incident wavelengths of 8, 9, and 11 Å were used to measure the NSE spectra with a dynamical range of 0.1 ns <

https://doi.org/10.1021/acsomega.5c04729
ACS Omega 2025, 10, 41446−41456

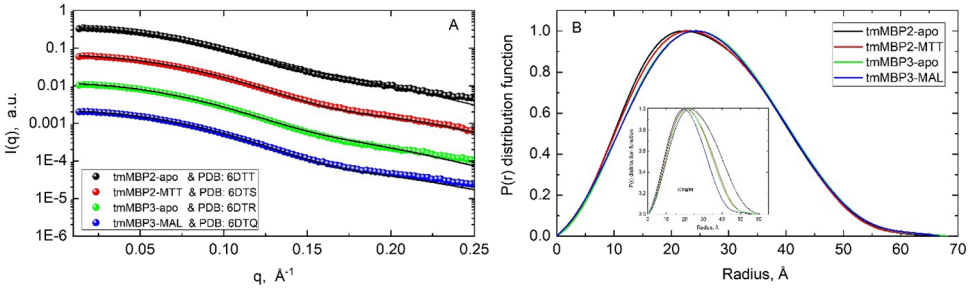

Figure 2. Small-angle neutron scattering (SANS) results of hydrogenated tmMBP2 and tmMBP3 @ 5 mg/mL in D_2O buffer. (A) Intensity vs q plot of tmMBP samples with their form factor fits shown as solid lines. *$I(q)$ data are logarithmically spaced for better visualization.* (B) Normalized $P(r)$ analysis of tmMBP proteins in the presence and absence of their cognate substrates, with the inset presenting the normalization of the high concentration (50 mg/mL) data.

τ_{max} < 130 ns (Fourier times) for q values ranging from 0.05 to 0.2 Å^{-1}. Data were also collected on dialysis D_2O buffer for background subtraction. Sample concentration was ∼51 mg/mL for all samples. All the experiments were performed in an enclosed sample environment at ∼50 °C. No sample aggregation or degradation was observed after a prolonged data collection time that extended over several days. Data reduction was performed using the DRSPINE[18,19] software package of the SNS-NSE instrument. Data analysis was performed using *Jscatter* software developed by Biehl.[20]

RESULTS AND DISCUSSION

Dynamical Substates in tmMBP's Revealed by Molecular Dynamics. MD simulations of apo- and substrate-bound tmMBP isoforms were performed for 500 ns. The aggregated root-mean-square fluctuations of top 10 slowest quasi-harmonic modes, RMSF10,[8] displayed in Figure 1A, and the quasi-harmonic top modes, QHA, displayed in Figure 1B, revealed distinct dynamical behaviors between tmMBP2 and tmMBP3. In tmMBP2, the apo form is more flexible, particularly in the C-terminal loop region interacting with the N-terminal domain (Region 1, Figure 1A), and N-terminal helices are near the binding site. Upon substrate binding, tmMBP2 becomes rigid, with some local fluctuations in exposed loop regions. QHA analysis confirms reduced overall dynamics but localized motion in tmMBP2. In contrast, tmMBP3 shows different dynamics, becoming more flexible upon substrate binding, particularly in the C-terminal loop near the binding site. In the apo form, this loop interacts with the N-terminal domain, but substrate binding disrupts this interaction. This loop modulates the protein's affinity for its substrate, stabilizing the open state in tmMBP3 and the closed state in tmMBP2. QHA calculations also show that there is differential fluctuation observed in tmMBP2 but not in tmMBP3.

Ten thousand (10,000) protein conformations from the last 100 ns of simulation time were averaged for each sample to create structural files (PDBs) later used for rigid body diffusion calculations and NSE scattering data analysis.

Conformation of tmMBP Isoforms in Solutions Revealed by SANS. Multiple SANS data sets were collected on both apo (tmMBP2-apo and tmMBP3-apo) and substrate-bound forms (tmMBP2-MTT and tmMBP3-MAL) at different protein concentrations to determine the effects of high concentration on the protein behavior in solution before the NSE experiment. The SANS data were fitted against the theoretically derived intensities of published crystal structures of tmMBP2 and tmMBP3, in both apo and holo-forms.[21,22] The solution scattering intensities and the theoretically derived intensities are in good agreement for the low concentration samples with minor variations for the high concentration solutions. The low concentration solutions of 5 mg/mL presented here in Figure 2A show a good representation of the form factor of tmMBP isoforms by their crystalline structures. The calculated $P(r)$ functions[12,23,24] of tmMBP's showed small variations in the radius of gyration (R_g) between the apo and the substrate-bound forms. The difference was larger between tmMBP2-apo (R_g = 19.87 Å) versus tmMBP2-MTT (R_g = 20.29 Å) than between tmMBP3-apo (R_g = 20.53 Å) versus substrate-bound form tmMBP3-MAL (R_g = 20.49 Å) (see Table 1).

Table 1. Radius of Gyration Derived from the $P(r)$ Analysis Method for the Low Concentration (5 mg/mL) and High Concentration (50 mg/mL) samples

sample name	R_g by P(r) analysis 5 mg/mL(Å)	R_g by P(r) analysis 50 mg/mL(Å)
tmMBP2-apo	19.87 ± 0.04	20.07 ± 0.02
tmMBP2-MTT	20.29 ± 0.02	20.23 ± 0.03
tmMBP3-apo	20.53 ± 0.04	20.63 ± 0.01
tmMBP3-MAL	20.49 ± 0.04	20.64 ± 0.04

The normalized $P(r)$ plot (Figure 2B) is an indicator of the overall compactness of the systems. At low concentration (5 mg/mL), all samples display similar compactness with both tmMBP3 samples slightly more expanded. At high concentration, 50 mg/mL, inset in Figure 2B, the tmMBP2-apo form is the least compact and most expanded protein, while the substrate-bound forms tmMBP2-MTT and tmMBP3-apo have similar compactness. At high concentration, the substrate-bound form of tmMBP3 is the most compact protein. Interestingly, the compactness of tmMBP3-apo is comparable to that of the substrate-bound form tmMBP2-MTT at 50 mg/mL.

The structure factor, $S(q)$, was calculated by dividing the high concentration scattering data by the low concentration form factor, for each of the four samples. An example is shown in Figure 3A for sample tmMBP3-apo. The calculated structure factors were fitted using the SASView program[25] (Figure 3B). tmMBP2-apo and tmMBP2-MTT structure factors were fitted by using the hard-sphere model. The model indicates less interaction with surrounding proteins, allowing faster particle diffusion, even in a crowded environment. On the other hand,

https://doi.org/10.1021/acsomega.5c04729
ACS Omega 2025, 10, 41446−41456

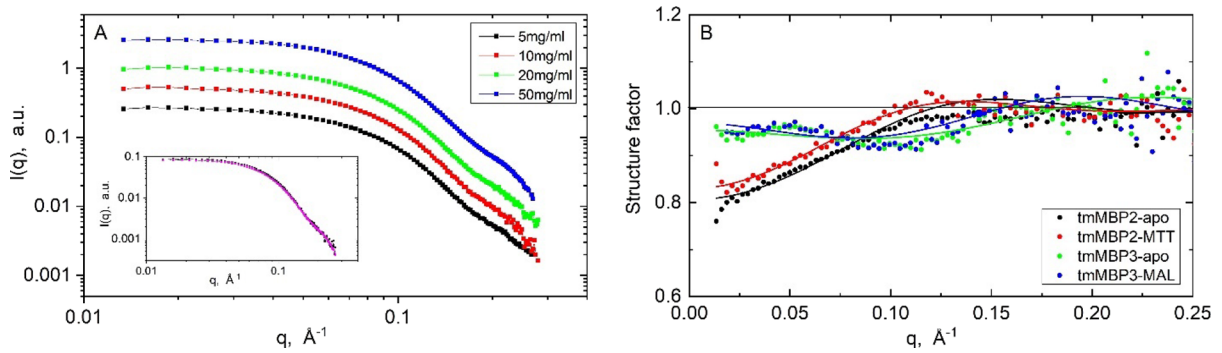

Figure 3. (A) Example of SANS data on dilution series, here for tmMBP3-apo, with the inset presenting the normalization of the high concentration (50 mg/mL) data by the low concentration (5 mg/mL) form factor. (B) Calculated structure factors fitted by hard-sphere models.

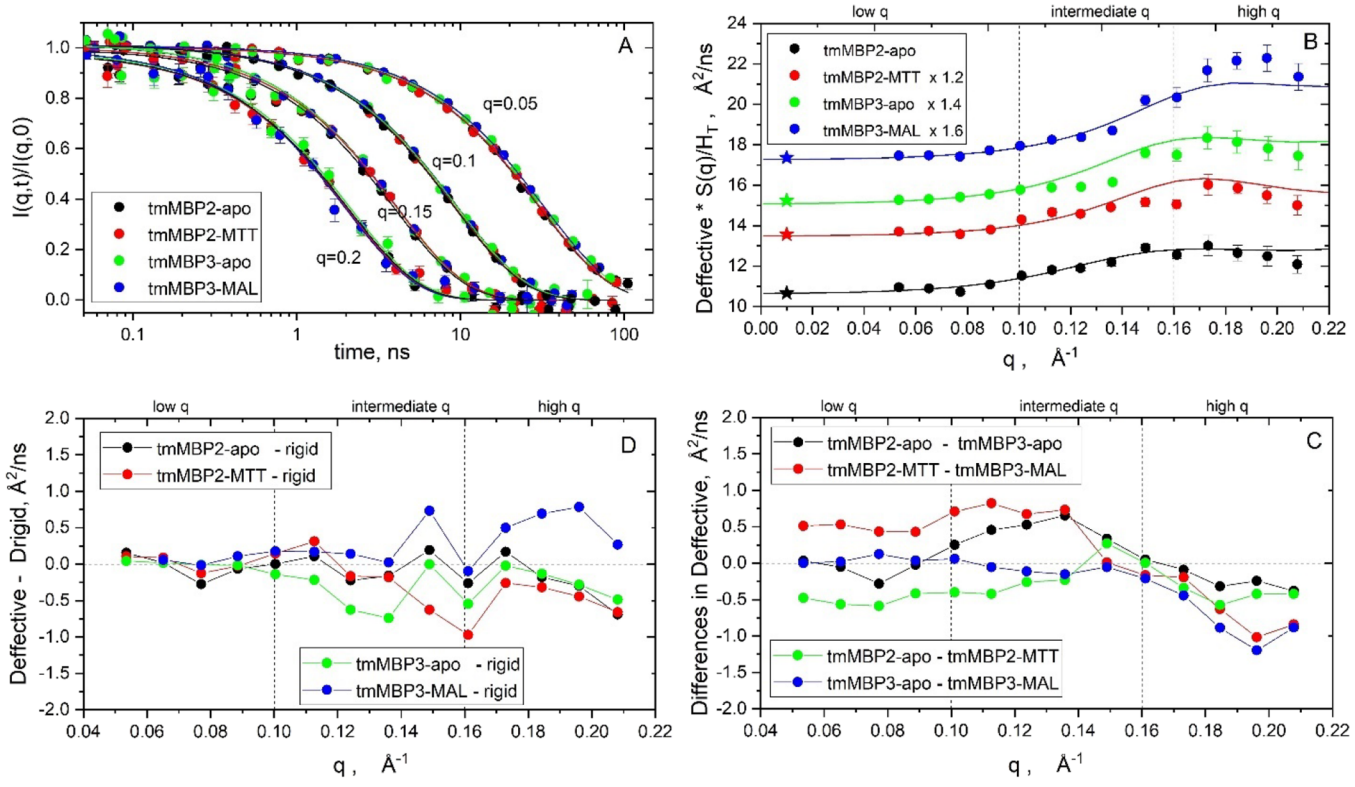

Figure 4. Neutron spin echo (NSE) data on tmMBP isoforms. (A) Intermediate scattering function $I(q, t)/I(q, 0)$ for four selected q values. Solid lines represent the single exponential fit. (B) Effective diffusion of tmMBP's as a function of q, corrected by structure factor and hydrodynamics. Solid lines are the scaled rigid body diffusion calculation, and the star symbols are the translational diffusion coefficients measured by DLS. Diffusion curves are shifted for better visualization with the factor marked on the figure. (C) The difference in effective diffusion between proteins isoforms. (D) The difference between experimental diffusion data and calculated rigid body diffusions. *The vertical dashed lines delimit the q-range (low, intermediate, high) and the horizontal dash lines are the lines of zero difference, i.e., equal effective diffusion.

the sticky-hard-sphere model was a better fit for the structure factor data from tmMBP3-apo and tmMBP3-MAL samples.

The sticky hard-sphere model calculates the hard-sphere model with a narrow, attractive potential well. The strength of its attractive well determines the extent of the "stickiness" of a particle and describes an increased interaction with surrounding molecules. Close inspection of the structure factor further indicates different protein−protein interaction behaviors of both isoforms and a significant difference in the structure factor of tmMBP2-apo vs tmMBP2-MTT at high concentration, possibly attributed to the more flexible nature of the apoprotein vs locked-down upon binding the MTT substrate. Minimal differences in the structure factor between the apo- and holo-states of tmMBP3 were noted. These results were also consistent with our previous findings on the flexibility of both isoforms[1] and reflected by the R_g values in Table 1. The calculated structure factors are essential for correcting the intermediate scattering function by the particle−particle interactions as strong interactions can affect the overall dynamics obtained from NSE measurements.

Dynamics of tmMBP Isoforms Revealed by NSE. The NSE experiments were performed on four samples, the apo and substrate-bound forms of tmMBP2 and tmMBP3 to quantify their pico-to-nanosecond solution-state dynamics in a noninvasive way. The intermediate scattering function $I(q, t)/I(q, 0)$ was measured up to $t \sim 100$ ns over a q-range of 0.05 to 0.2 Å^{-1}. The NSE data set was collected for the maximum q-range possible, close to the coherent-incoherent transition

https://doi.org/10.1021/acsomega.5c04729
ACS Omega 2025, 10, 41446−41456

Table 2. Results Parameters from HYDROPRO Calculations and Coarse-Grained Global Fit of the Intermediate Scattering Function

sample name	H_T	H_r	$Dt_{0\ \text{rigid HYDROPRO}}$ (Å^2/ns)	$Dr_{0\ \text{rigid HYDROPRO}}$ (1/ns)	$D_{0\ \text{DLS DLS}}$ (Å^2/ns)	internal relaxation time(ns)	Dt_0 (Å^2/ns)	χ^2	MSD (nm^2)
tmMBP2-apo	0.91	0.80	7.37	6.19×10^{-03}	10.66	12.32	8.48	5.63	5.33 ± 0.36
tmMBP2-MTT	0.89	0.80	7.42	6.52×10^{-03}	11.30	10.68	8.65	6.99	5.40 ± 0.32
tmMBP3-apo	0.87	0.80	7.31	6.22×10^{-03}	10.88	10.67	9.24	8.26	5.91 ± 0.29
tmMBP3-MAL	0.88	0.80	7.42	6.55×10^{-03}	10.85	26.45	10.70	4.29	3.60 ± 0.38

point of the sample, around q-value of ∼0.2 Å^{-1}. Each protein sample was concentrated to ∼50 mg/mL, and the temperature during the experiment was 50 °C. Figure 4A highlights four selected q values representing the low q-regime (0.05−0.1 Å^{-1}), the intermediate q-regime (0.1−0.16 Å^{-1}), and the high q-regime (0.16−0.2 Å^{-1}). As a first step in the analysis, the intermediate scattering function was fitted by the single exponential: $I(q, t)/I(q, 0) = \exp(-D_{\text{effective}} \cdot q^2 \cdot t)$ to calculate the effective diffusion coefficient $D_{\text{effective}}$.

From low q toward the high q, we transition from pure diffusive translational motions observed over the full range of relaxation time (up to 100 ns) toward the internal dynamics and segmental motions of the proteins, in the short time regime of several nanoseconds.[26] The signal decays faster from low q to high q (Figure 4A). The slower dynamics observed in the low q regime (q < 0.1 Å^{-1}) are dominated by the translational diffusive motions, which can take hundreds of nanoseconds to fully relax and represent collective motions for the molecules diffusing in the solvent. The intermediate q range (0.1− 0.16 Å^{-1}) shows a faster decay compared to the low q diffusive motions and is usually attributed to the rotational and tumbling motions of the proteins. Finally, the high q region (q > 0.16Å^{-1}) represents a "*zoomed-in view*" into the proteins' structures and dynamics and can reflect the flexibility of a particular secondary structure element or domain in the target protein, although translational and rotational diffusion are of course also visible.

The effective diffusion coefficient, $D_{\text{effective}}$, as a function of q presented in Figure 4B is a primeval estimation of the dynamic behavior of these samples. It encompasses translational and rotational motions, which are directly affected by the interparticle interactions, as well as the contributions from the internal dynamical modes directly affected by hydrodynamics. Therefore, the $D_{\text{effective}}$ has been corrected by the structure factor $S(q)$ derived from SANS measurements and by hydrodynamic interactions H_T (translational hydrodynamics factor), so that the corrected effective diffusion coefficient calculated for the lowest q matches the translational diffusion coefficient at q = 0 determined from DLS experiments (D_0). This correction yields the translational hydrodynamic factors, H_T, shown in Table 2. For this analysis, H_T was considered q-independent within the NSE window observed for each sample and was used as input value for further analysis by coarse grain modeling. Hydrodynamic effects on rotational diffusion are not considered at this point and are included in the modeling approach described further below. The effective diffusion analysis shows differences between samples quantified in Figure 4C and summarized as follows:

1. In the low q regime (<0.1 Å^{-1}), the apo form of both proteins, tmMBP2-apo and tmMBP3-apo, have similar diffusion coefficients. Binding tmMBP2-apo to MTT makes the complex diffusing faster (tmMBP2-MTT has higher diffusion coefficient than tmMBP2-apo) while tmMBP3-apo and the ligand-bound tmMBP3-MAL have almost identical diffusion coefficients. The difference between the two substrate-bound forms shows that tmMBP2-MTT is faster (higher diffusion) than tmMBP3-MAL.
2. Relaxation follows similar trends in the intermediate q regime (0.1−0.16 Å^{-1}) with the small difference that tmMBP2-apo seems to diffuse faster than tmMBP3-apo in this q range.
3. In the high q regime (>0.16 Å^{-1}), the dynamic is activated by substrate binding: tmMBP2-apo is slower than tmMBP2-MTT and tmMBP3-apo is slower than tmMBP3-MAL and the holo-form tmMBP2-MTT becomes slower than tmMBP3-MAL.

Upon ligand binding, tmMBP2-MTT gets faster than tmMBP2-apo and maintains almost constant difference at any given q range. This implies that mostly translation and rotation diffusion in tmMBP2 are affected in a similar way by the substrate presence. Upon substrate binding the protein structure gets more compact and uniform diffusing faster than its apo form. For tmMBP3 there is no dramatic change in the low and intermediate q range upon ligand binding. Differences in the rotational and internal q range (intermediate and high q's) pick up and become more pronounced for tmMBP3-MAL showing faster dynamics than its apo form. Some dynamic activation happens upon substrate binding of tmMBP3, and the protein suddenly shows the most prevalent motions between all four proteins showing the highest effective diffusion values.

Effective diffusion calculated from the NSE intermediate functions was compared to the protein rigid body diffusion calculated by the program HYDROPRO[27] using as protein structures input the pdb files averaged from 10,000 proteins conformations obtained from the last 100 ns of MD simulation time. The difference between the effective diffusion coefficient determined by NSE and the calculated rigid-body translational and rotational diffusion $\Delta D = D_{effective} - D_{rigid}$ is thought to indicate the presence of internal motions in the case that internal motions make a significant contribution to the NSE spectra. The calculated rigid body diffusion of the monomer as a function of q (solid lines in Figure 4B) describes well the experimental distribution of diffusion coefficients, when scaled to match the translational diffusion at q = 0 (D_0 obtained from DLS) by the factors in Table 2. Calculated rigid body diffusions show stronger differences in the intermediate-to-large q-range (>0.1 Å^{-1}) for all samples when compared to the NSE effective diffusion (Figure 4D), pointing toward variations in both structural flexibility and dynamics of the proteins as opposed to a simple rigid body motion. Again, the highest difference is observed for tmMBP3-MAL with a higher effective diffusion at q range >0.16 Å^{-1}. We note that

https://doi.org/10.1021/acsomega.5c04729
ACS Omega 2025, 10, 41446−41456

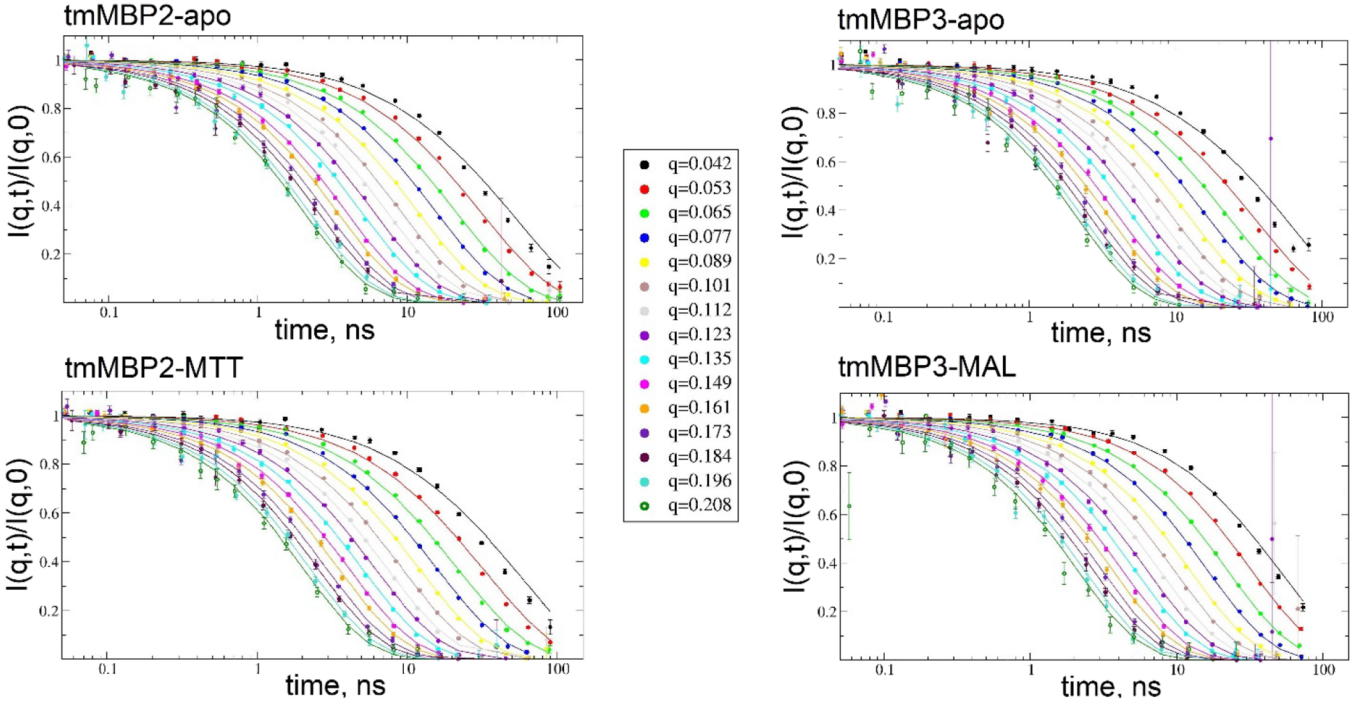

Figure 5. Global fit of translational, rotational, and internal dynamics for NSE intermediate scattering function $I(q, t)/I(q, 0)$ by a coarse grain model of 200 grains.

hydrodynamic effects on rotational diffusion have not been considered here, which can lead to an underestimation of the effective diffusion coefficients by NSE in the intermediate and high q range and mask the presence of internal protein dynamics in the ΔD plots.

In the next step, we analyze the $I(q, t)/I(q, 0)$ data by using an analytical model that considers both hydrodynamic effects on translational and rotational diffusion and includes additionally a contribution for internal protein dynamics. Values for the translational and rotational diffusion coefficients from rigid body calculation by HYDROPRO are collected in Table 2 and were used further as initial values for the analysis of the coherent intermediate scattering intensity. The intermediate scattering function, as stated before, has contributions from overall translational and rotational diffusions and motions within the molecule segments. We assumed that the full range of the relaxation function can be described by $I(q, t)/ I(q, 0) = I_{\text{translation}}(q, t) \cdot I_{\text{rotation}}(q, t) \cdot A_0 \cdot I_{\text{internal}}(q, t)$ where the internal protein dynamics part, $I_{\text{internal}}(q, t)$, is described by a q-independent relaxation rate Γ corresponding to a relaxation time $\tau = 1/\Gamma$ and a q-dependent amplitude $A(q)$ as given by $I_{\text{internal}}(q, t) = 1 - A(q) + A(q)\cdot\exp(-\Gamma t)$. This model has been successfully used to characterize the internal motions in various enzymes,[28−30] antibodies,[31] and transporter proteins[26] as well as intrinsically disordered proteins.[32,33] A global fit of all NSE spectra (Figure 5) was performed by coarse-grained structure-based calculations using structural PDB files obtained from the last 100 ns of MD simulation time for each sample, coarse-grained to 200 individual grains.

The model fits the translational diffusion coefficients Dt_0 as an indicator of the overall global motions, and the internal relaxation time and the amplitude of internal motions for each sample, while keeping as constant parameters the translational hydrodynamics factor, H_T equal to the values obtained from the correction of the effective diffusion D_{eff} by structure factors and hydrodynamics interaction (Figure 4B, Table 2), the rotational hydrodynamics factor fixed to H_r = 0.8, and the rotational diffusion coefficients fixed to the HYDROPRO rigid calculated values to ensure the convergency of the fit and avoid ill-posed problems due to large numbers of correlated parameters. The results of the global fit are displayed in Table 2 and Figure 5.

The coarse-grained model fits well the overall relaxation with the χ^2 values in Table 2. Three of the four samples relax with similar relaxation time, in the range of $\tau \sim 10$ ns, with tmMBP3-MAL exhibiting double the relaxation time, $\tau = 26.45$ ns. Using relaxation time as an indicator of how quickly the proteins return to equilibrium state (higher entropy state), this slower relaxation of tmMBP3-MAL can be attributed to the rigidity and compactness of the structure upon substrate binding. Similarly, the translational diffusion, $Dt0$, has the highest value for tmMBP3-MAL indicating faster translational motions. tmMBP3-MAL also has the fastest rotation: $Dr0$ is larger than the rest of the samples. A symmetrical and dense structure of the substrate bound tmMBP3-MAL is expected to translate and rotate faster in solution, acting like a compact rigid body, while asymmetry and expansions in the shape of the other tmMBP's structures shift the center of mass reducing tumbling and diffusive motions, with higher structural flexibility in general.

Amplitude of Internal Motions and Normal Modes Analysis. Normal Modes analysis in proteins refers to the collective motions that a protein can undergo, represented by specific motion patterns like bending, stretching, twisting, *etc.* Each normal mode has a frequency associated with it, which determines how fast these motion patterns are. Generally, the modes with lower vibrational frequencies correspond to slower and larger-scale motions, while higher-frequency modes correspond to faster and smaller-scale motions. The amplitude of internal motions resulting from coarse grain fit of the NSE

https://doi.org/10.1021/acsomega.5c04729
ACS Omega 2025, 10, 41446−41456

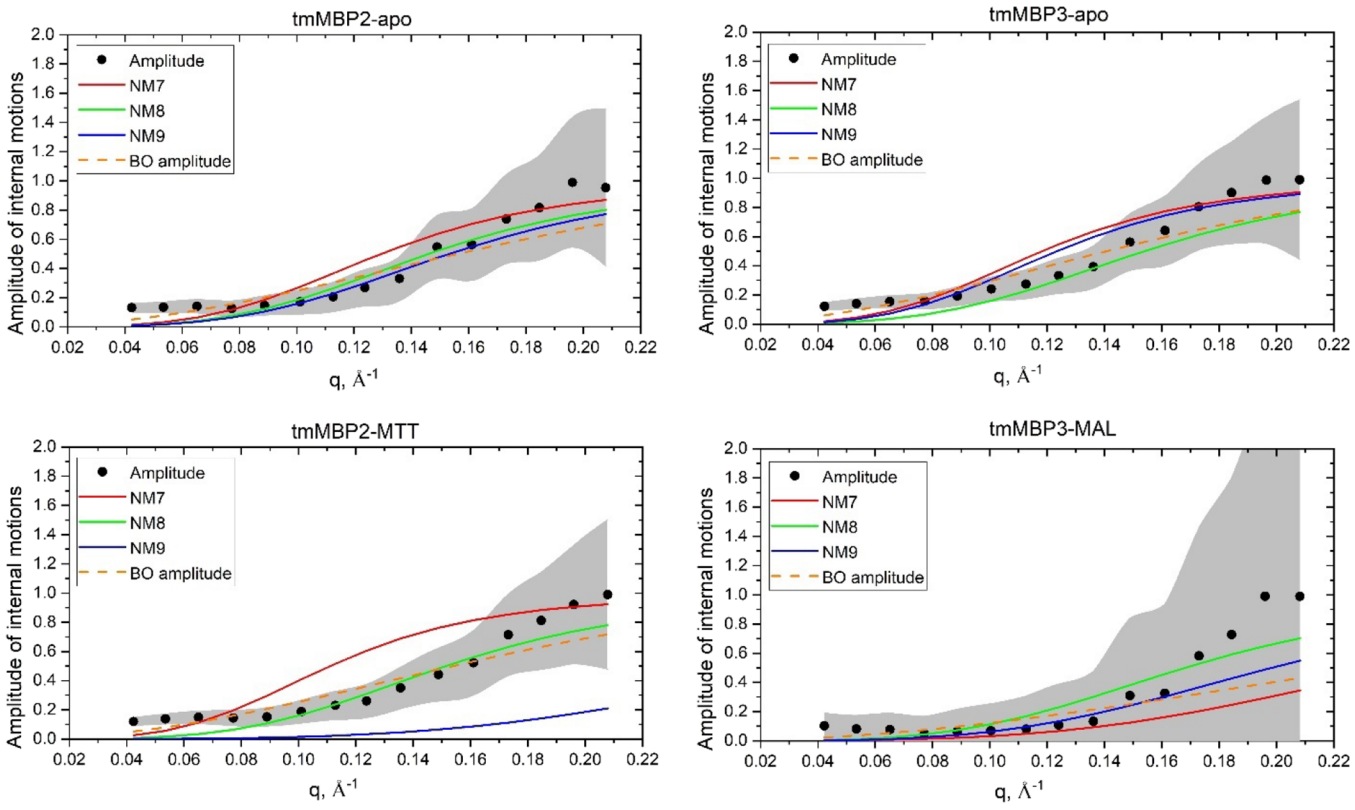

Figure 6. Amplitude of the internal motions contributing to the NSE relaxation spectrum. The amplitudes of the Normal Modes (NM7−NM9) are calculated using the PDB files from the last 100 ns of MD simulation time for each sample and displayed for comparison. Gray area represents the 1 sigma amplitude error interval. Dashed orange line is the amplitude fit by the exponential: $A(q) = 1 - \exp(-\langle u^2 \rangle \cdot q^2)$ where $\langle u^2 \rangle$ is the mean square displacement, equivalent to a Brownian Oscillator = BO amplitude.[26,34]

data for each sample is displayed in Figure 6 and, as a measure of the extent of internal dynamics, we compared this amplitude to the calculated amplitude prediction of the first three nontrivial Normal Modes, NM7 to NM9. At first glance, each sample exhibits individual amplitude characteristics as a function of q. Similarities in both values of the amplitude A and the shape of $A(q)$ can be seen for tmMBP2-apo and substrate bound tmMBP2-MTT. The tmMBP2-apo amplitude of internal motions is fairly described by both NM9 and NM8 amplitude, while the tmMBP2-MTT amplitude is generally best described by the NM8 amplitude mode.

Stronger differences are observed in the amplitude of the internal motions between tmMBP3 samples. While tmMBP3-apo displays amplitude values in the same range comparable to those of tmMBP2 samples (with NM8 amplitude mode best describing the overall trend), the shape of $A(\mathrm{i})$ is in general poorly described by any mode calculation. This could be attributed to differences in the structure between tmMBP2 and tmMBP3, which result in the binding to larger or smaller substrates within the same fold. Due to its significantly smaller binding pocket and due to the presence of steric hindrance near the substrate binding site in tmMBP3, the two domains open to only ∼35°. As a consequence of these shorter domain displacements, tmMBP3 in the apo form might resemble a transitional state intermediate of tmMBP2, somewhere between the fully open and the fully closed tmMBP2 forms. This becomes also evident from the SANS profiles analysis, where the radius of tmMBP2-MTT (R_g = 20.29 Å) is very close to tmMBP3-apo (R_g = 20.53 Å) (Figure 2B and Table1). Their internal relaxation times are also identical: 10.68 ns for tmMBP2-MTT and 10.67 ns for tmMBP3-apo, pointing toward similar structural flexibility. The most visible differences are observed in the amplitude of tmMBP3-MAL. Smaller amplitude values with larger errors as a function of q are calculated, with the NM9 amplitude best describing the behavior. The smaller amplitude values with large errors and higher frequency point toward annihilation of strong domain motions upon substrate binding no doubt due to the rigidity, compactness, and symmetric shape of the bound structure. This is also consistent with the slower relaxation and faster translational and rotation diffusive motions we observed experimentally in tmMBP3-MAL. In general, upon substrate binding, both proteins structures get more compact and uniformized, and stronger larger-scale domain motions are replaced by fast, high frequency, and small amplitude motion patterns.

Mean Square Displacements and Conformational Entropy. For binding substrates, thermal fluctuations are required within proteins to transition between different conformational states. The protein−substrate binding interaction is regulated, among others, by variations in the conformational entropy. The entropy difference between the two protein conformational states normalized per residue that participates in the observed motional processes, ΔS_{conf}/residue, can be estimated using the mean square displacement (MSD), which quantifies the amplitudes of average fluctuations within the protein structure:[34,35]

https://doi.org/10.1021/acsomega.5c04729
ACS Omega 2025, 10, 41446−41456

$$\Delta S_{conf}/\text{residue} = 3R\ln\left(\sqrt{\frac{MSD_{holo}}{MSD_{apo}}}\right) \quad (1)$$

where R is the universal gas constant. The calculated amplitude of internal motions contributing to the NSE relaxation from Figure 6 was described by an exponential function: $A(q) = 1 - \exp(-\langle u^2\rangle \cdot q^2)$, with $\langle u^2\rangle$ as the MSD in one direction.[34] The MSD values are listed in Table 2. MSD values for tmMBP2 in both apo and holo-forms are very similar (5.33 nm^2 and 5.4 nm^2) reinforcing the idea that the substrate binding has very little effect on the domain motions in tmMBP2, pointing slightly toward a plasticization of the structure. For tmMBP3-apo, a higher MDS is calculated (5.91 nm^2) as compared to tmMBP2-apo, showing more flexibility and domain dynamics in the ligand-free form of this protein. There is a significant reduction in the MSD value for tmMBP3-MAL (3.6 nm^2) and, therefore, in the effective amplitude of internal motions, pointing toward a strong reduction in flexibility of tmMBP3 upon substrate binding. Using the equation above, the difference in conformational entropy between holo-and apo states of tmMBP2 is ΔS_{conf}/residue = 0.174 ± 2.25 J/mol/residue, while in tmMBP3 is ΔS_{conf} /residue = −6.19 ± 2.93 J/mol/residue. Hence, in the time-and-length window of our NSE experiment, no significant change in conformational entropy of tmMBP2 is observed upon binding maltotetraose, while for tmMBP3, the maltose-binding strongly reduces the conformational entropy.

CONCLUSIVE REMARKS

Our study demonstrates how neutron scattering can detect and differentiate the dynamic profiles of structurally and functionally close-related isoforms upon ligand binding. The results suggest that structural similarity among tmMBP isoforms is complemented by differential dynamic modes that allow them to become functionally segregated. The NSE experiments enabled us to study the nature of these interactions and quantify their nanosecond solution-state dynamics across differing q and time-range, in both apo and holo-forms.

MD showed that upon substrate binding, tmMBP2 becomes rigid with reduced overall dynamics and some localized fluctuations in the exposed loop regions, which were also confirmed by the QHA analysis. In contrast, tmMBP3 became more flexible upon substrate binding.

The NSE results identified differences in the global motions of the two isoforms as well as in the segmental dynamics regime. From the NSE diffusion analysis, we conclude that upon binding MTT, the tmMBP2 structure gets more compact and uniform, diffusing faster than in apo form. The changes are even more pronounced for tmMBP3-MAL that exhibits the highest effective diffusion values. From the amplitude of internal motions and Normal Mode analysis, we reinforce the conclusion that upon substrate binding, protein structures tend to become more compact and rigid, where stronger and larger-scale domain motions are replaced by high frequency and small amplitude motion patterns, with the tmMBP3-MAL sample as the most rigidized conformation. The NSE results are supported by the $P(r)$ curves for the highly concentrated solutions where tmMBP3-MAL is the most compact state. This is the opposite of MD simulation and QHA analysis, which showed softening of tmMBP3. This discrepancy could stem from the fact that the MD simulations were performed with the NVE ensemble and might not reflect realistic thermodynamic conditions of the proteins. Another explication might be that the performed MD simulations and analysis methods are more sensitive to local changes around the ligand-binding pocket and do not probe the slow collective motional patterns that are detected by NSE. The amplitudes of motions of the simulated large-scale collective motions might be underestimated by MD and, hence, are difficult to detect in the simulations. Extended MD simulations up to the μs time range might be needed to allow for a direct comparison between the MD simulation and the NSE experiment.

No significant change in the conformational entropy of tmMBP2 is observed upon maltotetraose binding, while for tmMBP3 the maltose-binding reduces the conformational entropy. Speculating further, this indicates only small structural and dynamical changes in tmMBP2 upon ligand binding confined to some localized fluctuations with less affinity and binding specificity. Stronger reduction of the conformational entropy in tmMBP3-MAL points toward higher specificity and selectivity of tmMBP3, increased binding affinity toward MAL, reduction in the structural diversity of tmMBP3, and stability of the complex. This is consistent with the idea that the surrounding environment of a protein has either plasticizer or stabilizer effects and can allow or deny conformational sampling of proteins between conformational substates.

Correlating experimental dynamical signatures with molecular dynamics simulations to understand the conformational dynamics and ligand binding remains a significant challenge in biophysics. The role of conformational dynamics in molecular recognition is controversial, but future advancements in joint computational and experimental data analysis could lead to better energy resolutions, which could enable studies of even slower dynamical processes that form the basis of dynamics-coupled recognition mechanisms and conformational selection in proteins.

AUTHOR INFORMATION

Corresponding Author

Laura-Roxana Stingaciu − *Neutron Sciences Directorate, Oak Ridge National Laboratory, Oak Ridge, Tennessee 37831-2008, United States;* orcid.org/0000-0003-2696-5233; Email: stingaciulr@ornl.gov

Authors

Shantanu Shukla − *Vaccine and Infectious Disease Division, Fred Hutchinson Cancer Center, Seattle, Washington 98109-9024, United States;* orcid.org/0000-0002-5473-0207

Christopher Stanley − *Computing and Computational Science Directorate, Oak Ridge National Laboratory, Oak Ridge, Tennessee 37831-2008, United States;* orcid.org/0000-0002-4226-7710

Pratul Agarwal − *High Performance Computing Center, Oklahoma State University Stillwater, Stillwater, Oklahoma 74078-1010, United States;* orcid.org/0000-0002-3848-9492

Matthew Cuneo − *Department of Structural Biology, St. Jude Children's Research Hospital, Memphis, Tennessee 38105-3678, United States*

Andreas M. Stadler − *Jülich Centre for Neutron Science (JCNS-1), Forschungszentrum Julich GmbH, Jülich 52428, Germany; Institute of Physical Chemistry, RWTH Aachen University, Aachen 52056, Germany;* orcid.org/0000-0003-2272-5232

https://doi.org/10.1021/acsomega.5c04729
ACS Omega 2025, 10, 41446−41456

Dean Myles − *Neutron Sciences Directorate, Oak Ridge National Laboratory, Oak Ridge, Tennessee 37831-2008, United States*

Complete contact information is available at: https://pubs.acs.org/10.1021/acsomega.5c04729

Notes

The authors declare no competing financial interest.

■ ACKNOWLEDGMENTS

This research used resources at the Spallation Neutron Source, a DOE Office of Science User Facility operated by the Oak Ridge National Laboratory. The neutron beam time was allocated to BL-15 (SNS-NSE) and BL-6 (EQ-SANS) under proposal number IPTS-22579. The Office of Biological and Environmental Research supported research at the Center for Structural Molecular Biology (CSMB) at ORNL. P.K.A. acknowledges funding from NIH/NIGMS (R01 grant GM148886). The authors acknowledge R. Moody and Dr. K. Weiss for SNS biochemistry lab support. The D_2O used in this research was supplied by the United States Department of Energy Office of Science by the Isotope Program in the Office of Nuclear Physics.

■ REFERENCES

(1) Shukla, S.; Bafna, K.; Gullett, C.; Myles, D. A. A.; Agarwal, P. K.; Cuneo, M. J. Differential Substrate Recognition by Maltose Binding Proteins Influenced by Structure and Dynamics. *Biochemistry* **2018**, *57*, 5864.

(2) Gagné, D.; Narayanan, C.; Nguyen-Thi, N.; Roux, L. D.; Bernard, D. N.; Brunzelle, J. S.; Couture, J.-F.; Agarwal, P. K.; Doucet, N. Ligand Binding Enhances Millisecond Conformational Exchange in Xylanase B2 from Streptomyces Lividans. *Biochemistry* **2016**, *55*, 4184−4196.

(3) Case, D. A.; Cheatham, T. E.; Darden, T.; Gohlke, H.; Luo, R.; Merz, K. M. Jr.; Onufriev, A.; Simmerling, C.; Wang, B.; Woods, R. J. The Amber Biomolecular Simulation Programs. *J. Comput. Chem.* **2005**, *26*, 1668.

(4) Lee, J.; Hitzenberger, M.; Rieger, M.; Kern, N. R.; Zacharias, M.; Im, W. CHARMM-GUI Supports the Amber Force Fields. *J. Chem. Phys.* **2020**, *153*, No. 035103.

(5) Sciortino, F.; Fabbian, L.; Chen, S. H.; Tartaglia, P. Supercooled Water and the Kinetic Glass Transition. II. Collective Dynamics. *Phys. Rev. E: Stat. Phys., Plasmas, Fluids, Relat. Interdiscip. Top.* **1997**, *56*, 5397.

(6) Kamath, G.; Howell, E. E.; Agarwal, P. K. The Tail Wagging the Dog: Insights into Catalysis in R67 Dihydrofolate Reductase. *Biochemistry* **2010**, *49*, 9078−9088.

(7) Roe, D. R.; Cheatham, T. E. III PTRAJ and CPPTRAJ: Software for Processing and Analysis of Molecular Dynamics Trajectory Data. *J. Chem. Theory Comput.* **2013**, *9*, 3084.

(8) Ramanathan, A.; Agarwal, P. K. Computational Identification of Slow Conformational Fluctuations in Proteins. *J. Phys. Chem. B* **2009**, *113*, 16669−16680.

(9) Ezure, Y.; Marvo, S.; Kojima, M.; Sakai, T.; Yamamoto, H.; Tachikake, N.; Ogawa, H.; Toda, M. Manufacturing High Purity Maltose and Maltotetraose from Starch by a Novel and Efficient Procedure Named "Reducing End Modification Method. *Biosci., Biotechnol., Biochem.* **1997**, *61*, 1931.

(10) Sciortino, F.; Gallo, P.; Tartaglia, P.; Chen, S. H. Supercooled Water and the Kinetic Glass Transition. *Phys. Rev. E: Stat. Phys., Plasmas, Fluids, Relat. Interdiscip. Top.* **1996**, *54*, 6331.

(11) Zhao, J. K.; Gao, C. Y.; Liu, D. The Extended Q-Range Small-Angle Neutron Scattering Diffractometer at the SNS. *J. Appl. Crystallogr.* **2010**, *43*, 1068−1077.

(12) Svergun, D. I.; Koch, M. H. J. Small-Angle Scattering Studies of Biological Macromolecules in Solution. *Rep. Prog. Phys.* **2003**, *66*, 1735−1782.

(13) Konarev, P. V.; Petoukhov, M. V.; Volkov, V. V.; Svergun, D. I. ATSAS 2.1, a Program Package for Small-Angle Scattering Data Analysis. *J. Appl. Crystallogr.* **2006**, *39*, 277.

(14) Vanhoudt, J.; Clauwaert, J. Experimental Comparison of Fiber Receivers and a Pinhole Receiver for Dynamic and Static Light Scattering. *Langmuir* **1999**, *15*, 44.

(15) Babick, F. Dynamic Light Scattering (DLS). In *Characterization of Nanoparticles: Measurement Processes for Nanoparticles*; Elsevier: 2019.

(16) Stetefeld, J.; McKenna, S. A.; Patel, T. R. Dynamic Light Scattering: A Practical Guide and Applications in Biomedical Sciences. *Biophys. Rev.* **2016**, *8*, 409.

(17) Ohl, M.; Monkenbusch, M.; Arend, N.; Kozielewski, T.; Vehres, G.; Tiemann, C.; Butzek, M.; Soltner, H.; Giesen, U.; Achten, R.; et al. The Spin-Echo Spectrometer at the Spallation Neutron Source (SNS). *Nucl. Instruments Methods Phys. Res. Sect. A Accel. Spectrometers, Detect. Assoc. Equip.* **2012**, *696*, 85−99.

(18) Zolnierczuk, P. A.; Holderer, O.; Pasini, S.; Kozielewski, T.; Stingaciu, L. R.; Monkenbusch, M. Efficient Data Extraction from Neutron Time-of-Flight Spin-Echo Raw Data. *J. Appl. Crystallogr.* **2019**, *52*, 1022−1034.

(19) Zolnierczuk, P. A. *PySEN: A Python Package for Aiding Experiments at the SNS Neutron Spin Echo Spectrometer*; Oak Ridge National Laboratory: TN (United States), **2023**.

(20) Biehl, R. Jscatter, a Program for Evaluation and Analysis of Experimental Data. *PLoS One* **2019**, *14*, No. e0218789.

(21) Cuneo, M. J.; Changela, A.; Warren, J. J.; Beese, L. S.; Hellinga, H. W. The Crystal Structure of a Thermophilic Glucose Binding Protein Reveals Adaptations That Interconvert Mono and Di-Saccharide Binding Sites. *J. Mol. Biol.* **2006**, *362*, 259−270.

(22) Cuneo, M. J.; Changela, A.; Beese, L. S.; Hellinga, H. W. Structural Adaptations That Modulate Monosaccharide, Disaccharide, and Trisaccharide Specificities in Periplasmic Maltose-Binding Proteins. *J. Mol. Biol.* **2009**, *389*, 157−166.

(23) Svergun, D. I. Small-Angle Scattering Studies of Macromolecular Solutions. *J. Appl. Crystallogr.* **2007**, *40*, s10.

(24) Gräwert, M.; Svergun, D. A Beginner's Guide to Solution Small-Angle X-Ray Scattering (SAXS). *Biochemist* **2020**, *42*, 36.

(25) SASview, *Small Angle Scattering Analysis Software Package* Available online: http://www.sasview.org/.

(26) Ameseder, F.; Biehl, R.; Holderer, O.; Richter, D.; Stadler, A. M. Localised Contacts Lead to Nanosecond Hinge Motions in Dimeric Bovine Serum Albumin. *Phys. Chem. Chem. Phys.* **2019**, *21*, 18477.

(27) Ortega, A.; Amorós, D.; De La Torre, J. G. Prediction of Hydrodynamic and Other Solution Properties of Rigid Proteins from Atomic- and Residue-Level Models. *Biophys. J.* **2011**, *101*, 892.

(28) Biehl, R.; Hoffmann, B.; Monkenbusch, M.; Falus, P.; Préost, S.; Merkel, R.; Richter, D. Direct Observation of Correlated Interdomain Motion in Alcohol Dehydrogenase. *Phys. Rev. Lett.* **2008**, *101*, No. 138102.

(29) Monkenbusch, M.; Richter, D.; Biehl, R. Observation of Protein Domain Motions by Neutron Spectroscopy. *ChemPhysChem* **2010**, *11*, 1188.

(30) Inoue, R.; Biehl, R.; Rosenkranz, T.; Fitter, J.; Monkenbusch, M.; Radulescu, A.; Farago, B.; Richter, D. Large Domain Fluctuations on 50-Ns Timescale Enable Catalytic Activity in Phosphoglycerate Kinase. *Biophys. J.* **2010**, *99*, 2309.

(31) Stingaciu, L. R.; Ivanova, O.; Ohl, M.; Biehl, R.; Richter, D. Fast Antibody Fragment Motion: Flexible Linkers Act as Entropic Spring. *Sci. Rep.* **2016**, *6*, 22148.

(32) Stadler, A. M.; Stingaciu, L.; Radulescu, A.; Holderer, O.; Monkenbusch, M.; Biehl, R.; Richter, D. Internal Nanosecond Dynamics in the Intrinsically Disordered Myelin Basic Protein. *J. Am. Chem. Soc.* **2014**, *136*, 6987.

(33) Stingaciu, L. R.; Biehl, R.; Changwoo, D.; Richter, D.; Stadler, A. M. Reduced Internal Friction by Osmolyte Interaction in Intrinsically Disordered Myelin Basic Protein. *J. Phys. Chem. Lett.* **2020**, *11*, 292.
(34) Sarter, M.; Niether, D.; Koenig, B. W.; Lohstroh, W.; Zamponi, M.; Jalarvo, N. H.; Wiegand, S.; Fitter, J.; Stadler, A. M. Strong Adverse Contribution of Conformational Dynamics to Streptavidin-Biotin Binding. *J. Phys. Chem. B* **2020**, *124*, 324−335.
(35) Receveur, V.; Calmettes, P.; Smith, J. C.; Desmadril, M.; Coddens, G.; Durand, D. Picosecond Dynamical Changes on Denaturation of Yeast Phosphoglycerate Kinase Revealed by Quasielastic Neutron Scattering. *Proteins* **1997**, *28*, 380−387.

https://doi.org/10.1021/acsomega.5c04729
ACS Omega 2025, 10, 41446−41456